1   **Mapping seasonal glacier melt across the Hindu Kush Himalaya with time series SAR**

2   Corey Scher[1,2], Nicholas C. Steiner[2], Kyle C. McDonald[1,2,3]

3   [1]Department of Earth and Environmental Science, The Graduate Center, City University of New York, New York,
4   10031, United States
5
6   [2]Department of Earth and Atmospheric Science, The City College of New York, City University of New York, New
7   York, 10031, United States
8
9   [3]Carbon Cycle and Ecosystems Group, Jet Propulsion Laboratory, California Institute of Technology. 4800 Oak
10   Grove Drive, Pasadena. CA 91001, USA

11   *Correspondence to*: Nicholas C. Steiner (nsteiner@ccny.cuny.edu)

12   **Abstract.** Current observational data on Hindu Kush Himalayas (HKH) glaciers are sparse, and characterizations
13   of seasonal melt dynamics are limited. Time series synthetic aperture radar (SAR) imagery enables detection of
14   reach-scale glacier melt characteristics across continents. We analyze C-band Sentinel-1 A/B SAR time series data,
15   comprised of 32,741 Sentinel-1 A/B SAR images, determine the duration of seasonal glacier melting for 105,432
16   mapped glaciers (83,102 km^2 glacierized area), defined using optical observations, in the HKH across the calendar
17   years 2017-2019. Melt onset and duration are recorded at 90m spatial resolution and 12-day temporal repeat. All
18   glacier areas within the HKH exhibit some degree of melt. Melt signals persist for over half of the year at elevations
19   below 4,000 m a.s.l. and for nearly one quarter of the calendar year at elevations exceeding 7,000 m a.s.l. Retrievals
20   of seasonal melting span all elevation ranges of glacierized area in the HKH region, extending greater than 1km
21   above the maximum elevation of an interpolated 0ºC summer isotherm and at the top of Mount Everest, where *in*
22   *situ* data and surface energy balance models indicate the Khumbu glacier is melting at surface air temperatures
23   below -10ºC. Sentinel-1 melt retrievals reflect broad-scale trends in glacier mass balance across the region where the
24   duration of melt retrieved in the Western Himalaya and Karakoram is on average one month less than in the Eastern
25   Himalaya sub-region. Furthermore, percolation zones are apparent from meltwater retention indicated by delayed
26   refreeze. Time series SAR datasets are suitable to support operational monitoring of glacier surface melt and the
27   development and assessment of surface energy balance models of melt-driven ablation across the global cryosphere.

1   Introduction

29   Global warming driven by the anthropogenic release of geologic carbon is causing mass wasting of alpine
30   glaciers worldwide (Brangers et al.; Zemp et al., 2006). The Hindu Kush Himalaya (HKH) region, known
31   colloquially as the "Third Pole," has the most ice-covered area on Earth after the high-latitude polar regions (Yao et
32   al., 2012). In contrast to large ice sheets near the poles, these relatively small alpine glaciers – perched at some of
33   the highest elevations on Earth – are among the most sensitive indicators within the global cryosphere of changes in
34   global climate (Anthwal et al., 2006). Just as the recession of these sensitive mountain ice caps contributes to over
35   one quarter of global sea level rise (Zemp et al., 2019), disturbances accompanying HKH glacier retreat pose
36   innumerable hazards to humans and natural ecosystems. Glacier retreat threatens to disturb the dynamics of river

37 systems delivering freshwater resources to nearly 2 billion people across South and Central Asia (Brown et al.,
38 2007; Milner et al., 2017). Outburst floods resulting from glacier mass wasting have killed at least 6,300 people in
39 the Himalayas alone, and have caused extensive damage to property and livelihoods. These outbursts are expected to
40 increase in frequency with continued glacier wasting (Carrivick and Tweed, 2016). Some organisms endemic to
41 alpine aquatic ecosystems may become extinct as they lose biogeochemical regulation from upstream glaciers
42 (Jacobsen et al., 2012). As global temperatures rise and perennial snow and ice cover decreases, societies are faced
43 with difficult decisions around the costs and benefits of adapting to a changing climate within and around the HKH
44 region (Brown et al., 2007). Informed decision-making for successful climate change adaptation will require
45 knowledge of the state of natural systems and how these systems are projected to change alongside future increases
46 in population and global average temperature (Bogardi et al., 2012).

47   Substantial uncertainties exist in the current understanding of projected disturbances associated with a
48 changing climate, environment, and hydrologic regime across the greater Himalayas due to a lack of observations of
49 hydrology and meteorology at high elevations (Litt et al., 2019). The magnitude and rate of ablation from surface
50 melting is of particular importance as it drives changes in accumulation-zone snow-properties, such as percolation
51 and densification, that feedback into increased melting (Alexander et al., 2019). Surface melting has also been
52 linked to increased englacial temperatures resulting in faster ice motion (Miles et al., 2018). Although the general
53 trajectory of changes to the HKH cryosphere is understood (i.e. accelerated glacier mass loss on a decadal scale in
54 the Central and Eastern Himalaya), a consensus in projecting changes to HKH hydrology is lacking largely because
55 of missing *in situ* snow and ice monitoring data across these glaciated river basins (Fujita and Nuimura, 2011).
56 However, construction and maintenance of *in situ* monitoring station networks is costly and labor-intensive because
57 of the complexity of the high-mountain glaciated terrain. Satellite imaging radar retrieval of alpine glacier melt
58 characteristics has long been proposed as a source of data for hydrologic and glaciologic research (Shi et al., 1994).
59 Understanding of surface melting from observation records will enable advanced climate change projections of
60 glacier wasting that require snow property dynamics describing the retention, refreezing and drainage of liquid water
61 within glacier snow and firn (Pritchard et al., 2020).

62   Recent findings indicate that shortwave radiation drives melting at elevations where air temperatures are
63 perennially below freezing, such as those on Mount Everest where temperatures never exceed -10ºC (Matthews et
64 al., 2019; Matthews et al., 2020). These *in situ* findings indicate the degree to which temperature-indexed melt
65 models are underestimating ablation at these elevations using a 0ºC threshold for glacier melting. Further, studies of
66 glacier wasting in High Mountain Asia have shown variability in patterns and magnitude of glacier wasting across
67 sub-regions of the HKH that would be difficult to capture in numerical models using degree-day assumptions (Brun
68 et al., 2017). An observationally based dataset providing characteristics of the glacier surface energy balance is
69 necessary to capture seasonal and regional variability in glacier wasting across the HKH during melt-freeze cycles.
70

1.1 Snowmelt Detection and Radar Imaging

This study builds on extensive research on microwave scattering from dry and wet snow and associated techniques for snowmelt retrieval from imaging radar data to present an operational monitor for spatially-resolved glacier surface melt characteristics using synthetic aperture radar (SAR) time series and outlines of glacier area derived from satellite optical imagery across the HKH. Microwave remote sensing has been used to reliably monitor melt patterns across glaciers and ice sheets (Abdalati and Steffen, 2001; Ashcraft and Long, 2007; Jezek et al., 1994b; Steiner and Tedesco, 2014). Because imaging radar is independent of solar illumination and largely unaffected by cloud cover and atmospheric conditions, the fidelity of radar observations is defined by the frequency of the satellite platform's observational opportunities and by the characteristics of the imaging sensor. At C-band frequencies, frozen glacier percolation areas are recognized as one of the brightest radar targets on Earth, and glacier surfaces are unambiguous targets for determination of surface melt/freeze characteristics (Jezek et al., 1994; Rott and Mätzler, 1987). Detection of seasonal melt on ice surfaces at C-Band frequencies (4 – 8 GHz) depends on a strong radiometric response at melt onset (MO), when liquid water content introduced to an otherwise frozen snow or firn matrix causes a drastic decrease in the radar backscatter from the medium (Hallikainen et al., 1986). Deep, frozen snow and firn has a high scattering albedo across microwave frequencies (Matzler, 1998), resulting in high radar backscatter intensity over glaciated regions during the frozen months (Winsvold et al., 2018; Wiscombe and Warren, 1980). The introduction of liquid water in the snow or firn matrix at even hydrologically minimal amounts causes a pronounced increase in the medium's dielectric constant, increasing radar signal attenuation and diminishing volume scattering, and leading to a pronounced decrease in radar backscatter, usually by half power or more (Kendra et al., 1998; Shi and Dozier, 1995). In areas that are seasonally snow-free, *e.g.* for glacier ablation areas of debris-cover or bare ice, melting conditions are dominated by heterogeneous scattering mechanisms following the disappearance of seasonal snow, a topic of study not well represented in the theoretical literature on radar physics likely due to the complex nature of the glacier ablation surface. Because of the relatively strong signal produced at the onset of melting, radar-based melt-detection records have been developed across regions of the global cryosphere for several decades using both real and synthetic aperture radar sensors (Bhattacharya et al., 2009; Bindschadler et al., 1987; Koskinen et al., 1997). Subsequently, snowmelt detection algorithms have been developed using a host of radar sensors to monitor the onset and duration of snowmelt across glaciers and ice sheets (Abdalati and Steffen, 2001; Ashcraft and Long, 2007; Bahr et al., 1997; Jezek et al., 1994; Kayastha et al., 2019; Koskinen et al., 1997; Winebrenner et al., 1994). Prior applications of SAR mapping of seasonal surface melting over ice sheets and glaciers have been limited by a lack of repeat observations such as those now available from the Sentinel-1 SAR constellation (Lund et al., 2019).

Observations from time series SAR data have been used to delineate zones of glacier facies and regions of glacier mass balance (Winsvold et al., 2018). In glacier percolation zones, seasonally wet snow refreezes into ice lenses, pipes, and other percolation-related features that amplify both surface and volume scattering of C-band radar and result in the brightest SAR backscatter being captured during the frozen periods (Jezek et al., 1994; Rau et al., 2000). Studies have shown that SAR backscatter generally increases with elevation across glacier surfaces during frozen periods, from the glacier terminus, through frozen meltwater percolation zones, and eventually attenuating in

108 zones where dry snow accumulates (Winsvold et al., 2018). In transitions between these zones there are pronounced
109 backscatter contrasts rather than smooth, gradual transitions. At C-band frequencies, radar scattering within glacier
110 percolation areas dominates the backscatter amplitude during frozen periods (Jezek et al., 1994). Importantly for
111 melt ~~retirevals~~retrievals, the diminished volume scattering during surface melting in areas of meltwater percolation
112 creates a pronounced and unambiguous radar signature in time-series observations. The sensitivity of SAR
113 backscatter to the introduction of liquid water in an otherwise frozen snowpack or firn structure provides a reliable
114 mechanism for the retrieval of percolation zone melt characteristics (Lievens et al., 2019). In refreezing percolation
115 zones, the upper layers of firn will freeze first with the freezing front advancing downward across layers, thus
116 progressivly increasing backscatter and with decreasing total-column liquid water content (Ashcraft and Long,
117 2005). In this way, the timing of refreeze relative to the surface energy balance at the surface provides a direct and
118 spatially resolved indicator of subsurface meltwater storage within the snow or firn and deliniates the percolation
119 zones over mountain glaciers.
120   This study enlists SAR data acquired at a spatiotemporal resolution that captures melt variability across
121 mountain glacier surfaces suitable for constraining seasonal characteristics of melt onset and duration while building
122 on associated methods often employed for glaciers and ice sheets. In this paper we utilize SAR data to retrieve melt
123 status on HKH glacier surfaces with a simple threshold-based change detection classification melt/freeze state - an
124 observational constraint on the surface energy balance. It is likely that intense incident solar radiation is driving
125 these melt processes at elevations above the 0ºC summer isotherm (Matthews et al., 2019) across the entirety of the
126 HKH, and that the sensitivity of SAR backscatter to changes in the glacier surface melt/freeze condition as seen
127 when water transitions between solid and liquid phases provides a real alternative to temperature elevation lapse rate
128 estimates of melting (Litt et al., 2019) for assessing surface energy balance models of glacier ablation. Though
129 coarse in temporal resolution relative to typical meteorological datasets, retrieval of melt status using SAR time
130 series produces mappings with very high spatial resolution and a continuous record of melt timing and duration
131 across glaciated regions. We present an application of this melt retrieval technique at the scale of the HKH with
132 spatiotemporal fidelity adequate to capture seasonal variability in melt timing and duration across individual glacier
133 surfaces and capture sub-regional heterogeneities across the HKH.

2   Setting and Data

135   The HKH region (*Fig. 1*) spans 13 million km^2, including areas inhabited by 240 million people with nearly
136 2 billion people relying on the delivery of water resources from catchments that originate within the region (Scott et
137 al., 2019). Within the high elevation HKH, seasonal meltwater from snow and glacier ice is the primary source of
138 domestic freshwater supply (Bolch et al., 2012). Wasting of HKH glaciers poses a risk to the domestic water
139 resources supply for those populations living within these high elevation HKH catchments (Wood et al., 2020).
140 Glacier wasting in the HKH is heterogeneous; increases in global average temperature have caused wasting of
141 mountain glaciers across all HKH sub-regions, save the eastern Karakoram, Kunlun Shan, and adjacent sub-regions
142 at the intersection of South and Central Asia (Gardelle et al., 2012). Distinct glacio-climatic sub-regions are
143 characterized by these unique dynamics of glacier wasting (Bolch et al., 2019a). The wasting of HKH glaciers is

144 thus a spatially and temporally heterogeneous phenomenon where distinct glacio-climatic regimes control ablation

145 (Bolch et al., 2012). In this study, we refer to glacio-climate sub-regions delineated in Bolch, et al. (2019a) and

146 modified by Shean, et al. (2020). These delineations of glacio-climate were produced by the Hindu Kush Himalaya

147 Monitoring and Assessment Program (HiMAP) and we will refer to the sub-regional delineations as "HiMAP

148 regions" throughout the text. We selected 17 HiMAP subregions that intersected with a boundary of the HKH region

149 delineated by the International enter for Integrated Mountain Development (ICIMOD). The HKH region, HiMAP

150 sub-regions, and glaciated area summaries within each HiMAP sub-region are illustrated in *Fig. 1* alongside

151 Sentinel-1 acquisition plan.
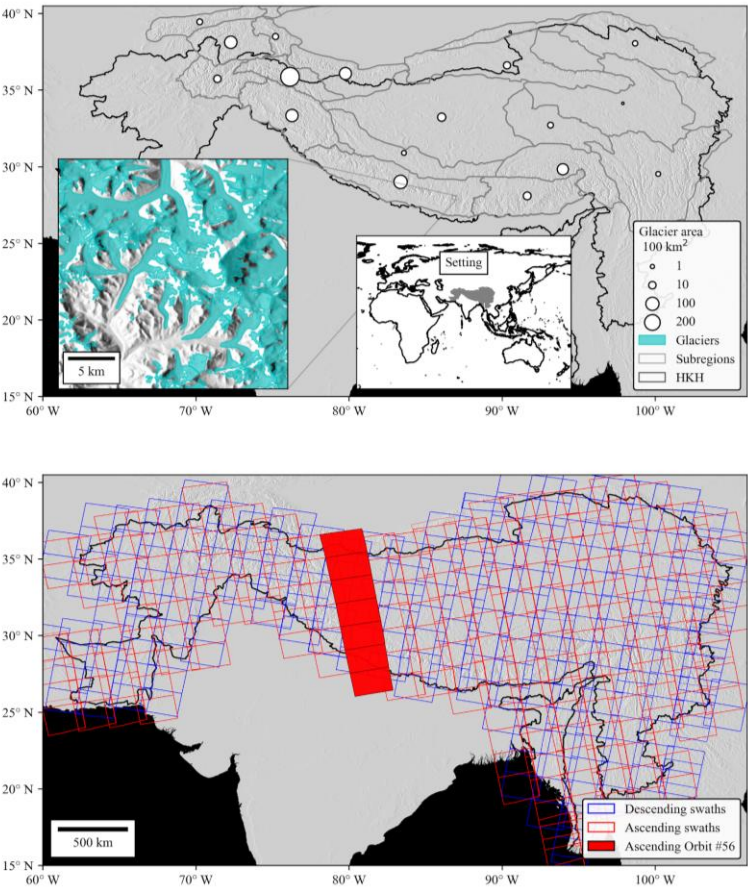
152
153 **Figure 1. (Top)** Hindu Kush Himalaya (HKH) region and 2018 GAMDAM glacierized areas summed across
154 glacio-climate sub-regions from Shean, et al. (2020). An inset map highlights the spatial fidelity of GAMDAM
155 outlines in the top panel. GGI and HKH data overlay a 30m Shuttle Radar Topography Mission (SRTM) DEM
156 hillshade (Farr, 2007a). **(Bottom)** Sentinel-1 ascending (red) and descending (blue) swath footprints acquired across

157 the study region. Ascending orbit cycle number 56 is highlighted in red to illustrate the SAR image processing
158 approach for time series analysis across distinct orbit cycles.

2.1 GAMDAM Glacier inventory (GGI)

160   The Glacier Area Mapping for Discharge from the Asian Mountains (GAMDAM) glacier inventory (GGI) is
161 a contemporary (July 2019) database on glacier outlines for the region of High Mountain Asia (*Fig. 1*). These
162 outlines were originally delineated automatically using cloud and snow-free satellite optical imagery in an initial
163 release of the database (Nuimura et al., 2015). As a recent update to the database, each outline was individually
164 inspected for quality control to correct discrepancies where automatic glacier delineation lost accuracy in terrain-
165 occluded areas, at debris covered portions of glaciers, and through obstruction under seasonal snowpack. The
166 recently updated glacier outlines were derived from satellite optical imagery captured across the HKH by Landsat 5
167 and 7 between 1990-2010 (Sakai, 2019). Although these data are the most current in terms of quality control
168 spanning the study region, they do not necessarily capture debris-covered portions of glaciers due to confusion with
169 land in optical image classification schemes; an issue that may be resolved with interferometric SAR phase
170 decorrelation (Bolch et al., 2019b). The 2018 GAMDAM database contained within the HiMAP sub-regions
171 includes 105,432 distinct glacier outlines spanning a total area of 83,102 km^2 within the HKH (Nuimura et al.,
172 2015).

2.2 Sentinel-1 Synthetic Aperture Radar

174   The Sentinel-1 A/B satellites were launched in April of 2014 and 2016, respectively, and collect C-band
175 (5.405 GHz) SAR data with a combined revisit interval of 6-days over of the majority of the terrestrial Earth. Each
176 Sentinel-1 scene acquired in the interferometric wide-swath (IW) mode has a width of 250 km and a resolution of
177 5x20 meters in range and azimuth at the equator. This study utilized images taken in the IW mode and in cross-
178 polarized state (VH). Sentinel-1 data were accessed through a cloud-computing platform (discussed below) wherein
179 SAR scenes were radiometrically terrain corrected to backscatter intensity values in decibels (dB) using the
180 European Space Agency's (ESA) Sentinel Application Platform (SNAP) toolbox and the Shuttle Radar Topography
181 Mission (SRTM) 30m digital elevation model (DEM) (Farr, 2007) upon ingestion into the cloud environment. Data
182 from both the ascending and descending orbit nodes were analyzed across the study region for a total consideration
183 of 32,741 individual Sentinel-1 A/B IW scenes across 46 unique orbit cycles captured across the calendar years
184 2017-2019 *(Table 1, Fig. 1b)*. By combining orbit directions, we utilize observations acquired at day and night. For
185 the purpose of this study we do not attempt to resolve diurnal-scale melt-freeze processes and instead focus on
186 retrieving seasonal and annual characteristics of melt timing and duration. Cross-polarized SAR backscatter
187 provides enhanced observational sensitivity to volume scattering of the radar signal in deep, dense and weathered
188 snowpack and firn (Rott and Mätzler, 1987). We selected cross-polarized (VH) Sentinel-1 A/B observations because
189 VH data show less angular sensitivities to contrasts between dry and wet snow (Nagler et al., 2016). Cross-polarized
190 Sentinel-1 SAR did not become available over the HKH until early 2017 and thus restricted this study timeframe. As
191 illustrated in *Fig. 2*, we observe a large (>3dB) difference in the seasonal radar backscatter between frozen and
192 melting conditions across the entirety of glacier surfaces in cross-polarized (VH) SAR data.

193
194 **Table 1.** Sentinel-1 image count and orbit paths used in this study.

Orbit Direction	Number of S-1 Images by Year			Relative orbit cycle
	2017	2018	2019	
Descending	4,424	5,436	5,253	4, 5, 19, 20, 33, 34, 48, 49, 62, 63, 77, 78, 92, 106, 107, 121, 122, 135, 136, 150, 151, 164, 165
Ascending	5,302	6,097	6,150	12, 13, 26, 27, 41, 42, 55, 56, 70, 71, 85, 86, 99, 100, 114, 115, 128, 129, 143, 144, 158, 172, 173

195
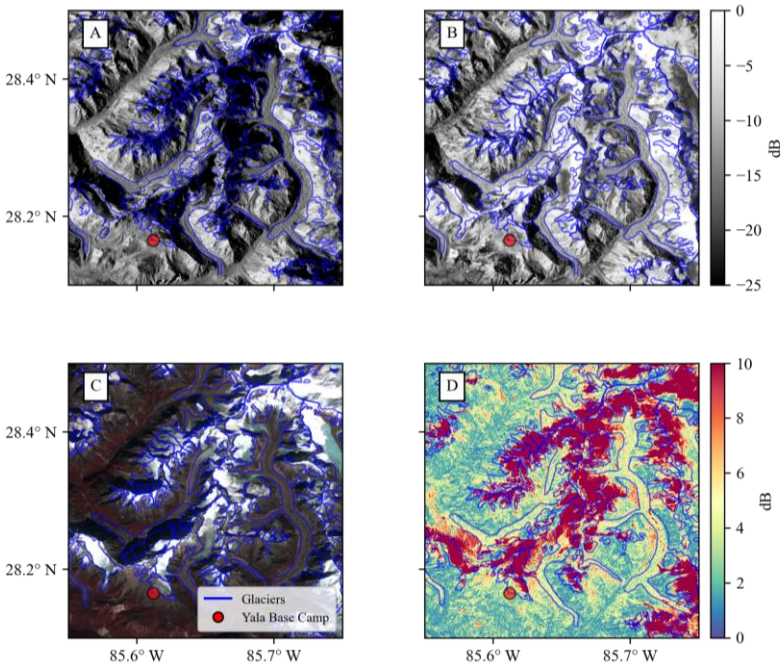
196
197 **Figure 2. (A)** Mean summer (July-August) 2018 cross-polarized (VH) backscatter across an example region in the
198 Trishuli basin, Nepal. **(B)** Mean 2018 winter (January- February) VH backscatter from Sentinel-1. **(C)** Sentinel-2
199 false-color (near-infrared, green, blue) image acquired by Sentinel-2 on October 30, 2018. Glacier outlines are
200 shown in blue and the Yala glacier base camp meteorological station is marked in red. Note the snow covered and
201 bare-ice portions of outlined glaciers and other debris-covered portions of glacier ablation areas. **(D)** The difference
202 between mean summer and winter VH backscatter from Sentinel-1.
203

2.3 Computing Infrastructure

A cloud-computing platform and application programming interface with pre-processed radiometrically terrain corrected Sentinel-1 A/B data was used to detect melt characteristics across the region (Gorelick et al., 2017). Radiometric terrain correction of Sentinel-1 data was conducted upon ingestion to the cloud server using the ESA's method contained within the Sentinel Applications Platform (SNAP) processing toolbox. The SNAP toolbox is used for Sentinel-1 images to update orbit metadata with restituted orbit files, remove invalid edge data and low intensity noise, remove thermal noise, compute σ^0 backscatter, and conduct orthorectification upon ingestion of data to the server (Google, 2020). The SNAP toolbox terrain correction functionality utilizes the 30m spatial resolution SRTM DEM (Farr, 2007; Margulis et al., 2019). The pre-processed SAR times series data and API functionality used to derive glacier melting characteristics are available from Google Earth Engine and can be used to recreate the work presented in this study.

2.4 Automated Weather Station Data

Measurements from two automated weather stations (AWS) are used to estimate surface energy balance (SEB) and evaluate surface melting conditions over high elevation glaciers. The Camp II (27.9810°N, 86.9023°E, 6,464 m a.s.l.) and the South Col (27.9719°N, 86.9295°E, 7,945 m a.s.l) AWS were installed around Mount Everest, Nepal as part of the National Geographic and Rolex Perpetual Planet Expedition to Mt. Everest in April-May 2019 (Matthews et al., 2019). Measurements were collected at an hourly interval and include air temperature, wind speed, relative humidity, incoming shortwave and longwave radiation and barometric pressure. Time series plots of meteorological observations are shown in *Supplementary Information Fig. S1*. Please see Matthews et al. (2020) for a complete description of sensor specifications and sampling interval.

3 Methods

3.1 Melt Classification

We use a threshold-based change detection algorithm applied to time series radar backscatter intensity to classify melt conditions (Ashcraft and Long, 2007). Melt detection is conducted across Sentinel-1 A/B ascending and descending orbit track time series separately and mosaicked into a final image based on a statistical score for seasonal melt magnitude after classification. To classify snowmelt, we conduct a pixel-based temporal classification by comparing each image at interval i to a dry/frozen winter average backscatter value calculated from January to February for each study year. Due to missing VH acquisitions at some locations during the 2017 frozen months, (Jan – Feb) we utilized 2018 frozen month reference data for melt retrieval across the calendar year 2017, as regular acquisitions across the HKH began in late February 2017. Snowmelt at each image acquisition interval (m_i) was classified using *Eq. (1):*

236
$$m_i = \begin{cases} 1, & if \ \sigma^0_i < \bar{\sigma}^0_w - b, \\ 0, & if \ \sigma^0_i > \bar{\sigma}^0_w - b. \end{cases} \qquad (1)$$

237

238   where the ground-range detected backscatter intensity at each image acquisition (σ^0_i) within the times series must

239   be less than the difference between the mean winter backscatter $(\bar{\sigma}^0_w)$ and a fixed threshold (b). Threshold values

240   (b) have been developed across numerous studies of melt detection with C-band scatterometer and SAR datasets

241   using both ground-based observations and radar scattering model results of changes to backscatter magnitude at the

242   onset of melt. We followed previous studies (Baghdadi et al., 1997; Bhattacharya et al., 2009; Engeset et al., 2002;

243   Nagler and Rott, 2000; Oza et al., 2011; Rott and Mätzler, 1987; Steiner and Tedesco, 2014; Trusel et al., 2012) and

244   selected a b value equal to one half of the signal power (-3 dB). *Figure 3* provides an illustration of the SAR melt

245   signal for a high elevation (4,950m a.s.l) meteorological station, located at the Yala glacier base camp. Backscatter

246   values averaged across the Yala glacier acquired along the Sentinel-1 A/B descending orbit direction are plotted

247   alongside mean daily air temperature recorded at the Yala glacier base camp automatic weather station (Shea, 2016).

248   If we consider air temperature above 0ºC to control glacier surface melt at this location, classification accuracy for

249   melt retrieval using *Eq. (1)* is 96% in the VH polarization.
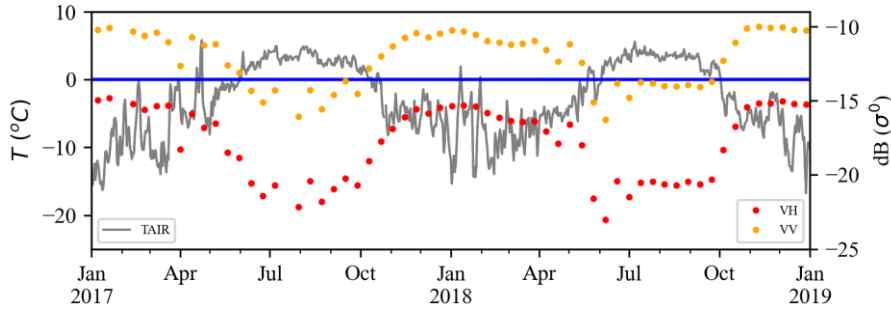
250
251   **Figure 3.** Time-series chart of air temperature measured at the Yala glacier base camp (4,950 m a.s.l) and Sentinel-1
252   A/B descending backscatter averaged across the Yala glacier for the years 2017-2018. Assessment of algorithm
253   performance assuming mean daily air temperatures above 0ºC indicates active melt results in 96% accuracy for melt
254   classification across this time series in the VH polarized backscatter.

255   ## 3.2   Quantifying algorithm performance

256   Sentinel-1 SAR viewing geometry will vary as the local incidence angle increases with across-track range. At

257   high incidence angles (far range), the sensitivity to volume scatter is diminished and the melting signal is reduced.

258   At C-band frequencies, these effects on volume scatter are strongest only at very high incidence angles (closer to

259   grazing) (Nagler and Rott, 2000). We classified areas as valid for melt detection using a metric of statistical

260   separability for seasonal backscatter intensity across frozen and melt periods, which we interpret as a measure of the

261   strength of the seasonal melt signal *Eq. (2)*:

262

263
$$z = \frac{\bar{\sigma}^0{}_w - \bar{\sigma}^0{}_s}{s(\sigma^0{}_w)},$$ (2)

264

265   where the score for seasonal separability of backscatter intensity (z) was calculated across each SAR pixel's time

266   series using the difference between the mean winter $\bar{\sigma}^0{}_w$ (January-February) and summer $\bar{\sigma}^0{}_s$ (July-August) season

267   backscatter intensities, as compared to the standard deviation of backscatter across the winter months $s(\sigma^0{}_w)$. In

268   computing z, we employed consistent repeat-pass observation geometries thereby allowing application of the time

269   series melt-detection algorithm in regions of complex terrain. This metric serves as a measure of the magnitude of

270   the seasonal melt signal across each pixel's time series. It is used here as a criterion to identify valid melt

271   observations and for selection of pixels employed in regions of overlapping orbital tracks, based on the sensitivity of

272   the radar backscatter to melting. We apply this metric to choose which orbit direction (ascending or descending) to

273   use for melt classification on a per-pixel basis after applying *Eq. (1)* across each orbit cycle time series, so as to

274   capture the maximum area of melt signals occurring across the complex terrain.

275   Sentinel-1 A/B interferometric wide (IW) swath images have a range in viewing angle between 29.1-46.0°

276   (ESA). Glacier melt retrieval using SAR data commonly begins with a normalization of radar images by viewing

277   angle on a scene by scene basis (Adam et al., 1997; Huang et al., 2011; Rott and Mätzler, 1987; Winsvold et al.,

278   2018). We consider changes for each individual orthorectified 10x10m pixel time series across distinct, repeating

279   orbit tracks and directions. This approach holds the local incidence angle effectively constant for each region

280   observed by a given set of orbit tracks. Glacier melt classification and **z**-score calculation are carried out across

281   images acquired along identical orbit tracks in distinct orbit directions (*Fig. 1*) and mosaicked into a final dataset for

282   each study year using the greatest **z**-score observed across each orbit cycle path and in each orbit direction. We thus

283   limit temporal resolution of melt retrievals to 12-days by choosing only observations from the orbit direction with

284   the greater **z**-score on a per-pixel basis. Time series analysis of SAR acquisitions on distinct orbit tracks eliminates

285   the need to normalize each scene by incidence angle for the purposes of melt retrieval. This method reduces

286   computational cost and eliminates artefacts that may originate from overlapping orbit paths and differences in radar

287   viewing angle. Areas where complex topography controls the backscatter should show little time series variability in

288   backscatter change at the SAR pixel scale when viewed at a distinct and consistent orbit path and direction and

289   should not pass the **z** score test.

290   We apply time series melt detection only where inter-seasonal backscatter intensities are separated by

291   greater than two standard deviations ($z > 2$), representing better than 98% confidence in the presence of an annual

292   melt signal. For all locations, the orbit direction and orbit cycle that has the greatest **z** value is used for melt

293   classification. We find that **z** generally increases with elevation across sub-regions of the HKH and that, across

294   elevation ranges, the mean **z** is above the threshold for melt retrieval, indicating detection of a seasonal melt signal

295   across all ranges of glacier elevation spanning the HKH (*Fig. 4*). Areas of debris-cover may exhibit radar

296   brightening with snow-free conditions above winter mean ($z < 0$). These areas occur towards lower elevations

297   where seasonal snow, or firn, does not have significant contribution to the seasonal backscatter response and are not

298   included in our melt classification approach following **z**-score thresholding. Nonetheless, there exists retrievable

299   melt signals (i.e. $z > 2$) across ablation surfaces such that median window filtering across ablation zones can result

300   in a geospatial dataset with more complete coverage. We obtain more robust estimates of melting onset and refreeze

301   by spatially aggregating results of the glacier surface melt timing (*Eq. 1*) using a median window filter of 9x9 pixels

302   after melt classification and **z**-score validation. Reach-scale regions where SAR signals fail the **z**-score test are thus

303   interpolated over using 9x9 pixel median window filtering. The complexity of SAR signals involves the diverse

304   scattering mechanisms on ablation surfaces following the disappearance of seasonal snow. Because sufficient data is

305   retrievable on ablation surfaces (i.e. **z** > 2), median window filtering enables greater spatial continuity in SAR-

306   derived melt retrieval data. All spatiotemporal characteristics we report herein are after median window filtering of

307   melt retrievals from 10m native resolution to 90m resolution. In *Fig. 4* we show the mean **z** across HiMAP sub-

308   regions in order to illustrate that, on average, even where debris-covered portions of glaciers may exhibit an inverse

309   response to melt with the disappearance of snow, Sentinel-1 records a mean **z** indicative of a seasonal snowmelt

310   signal across all elevation ranges of glaciation. Mean seasonal melt magnitude averaged over 100m elevation bins

311   over all three calendar years of data shows strong (**z** > 2) melt signals across glacio-climatic sub-regions and across

312   all elevation ranges of significant glaciation (*Fig. 4*).
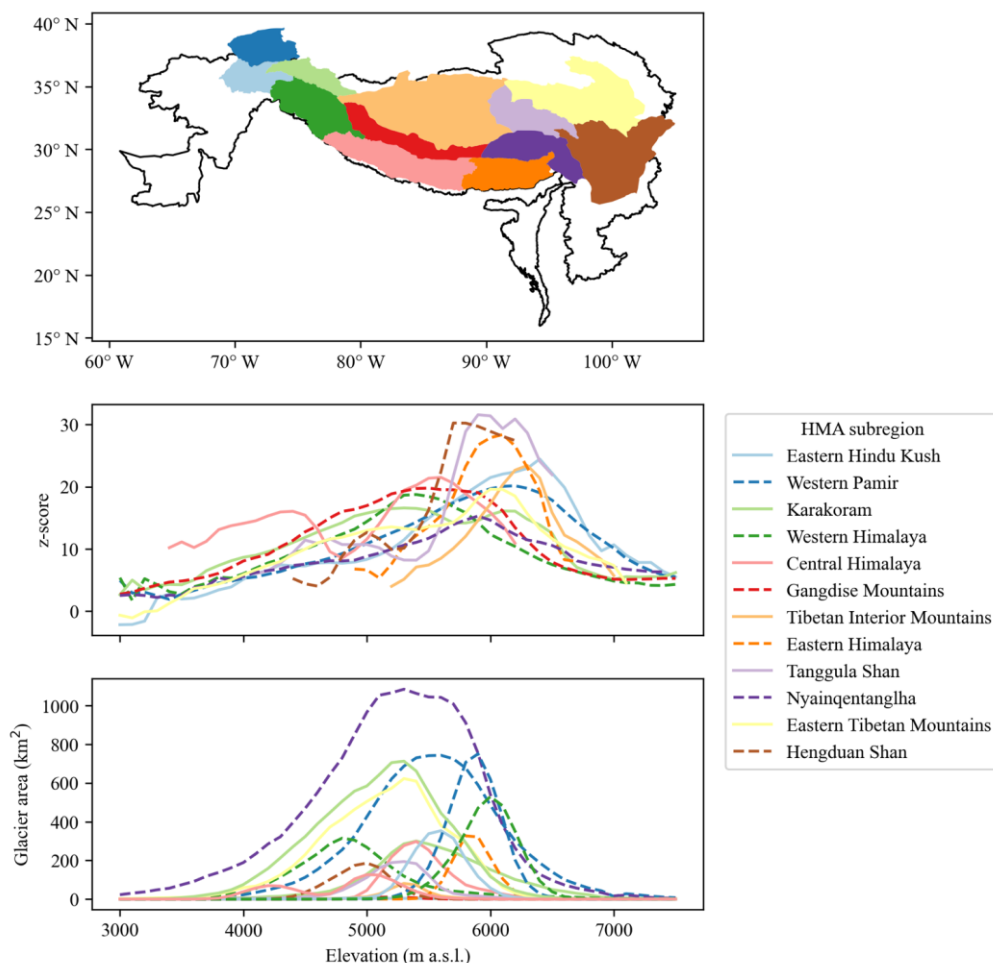
313
314 **Figure 4. (Top)** Glacio-climate sub-regions within the Hindu Kush Himalaya codified in Shean, et al. (2020).
315 **(Middle)** Mean z-score (2017-2019) by 100m SRTM elevation bin over each sub-region in the HKH. **(Bottom)**
316 Mapped glacier area from the GAMDAM database (Sakai, 2019) over 100m SRTM (Farr, 2007) elevation bins for
317 each sub-region.

3.3   Surface Energy Balance and Surface Melting

319   Sentinel-1 SAR (S1-SAR) detects a substantial area and duration of melting at elevations where air

320 temperatures should be well below freezing. Although measurement data in these areas are scarce, AWS installed

321 during 2019 at Mt Everest Nepal can provide two instances of point-scale validations of glacier melting using

322 surface energy balance (SEB) modelling based on *in situ* measurements. As described in Matthews et al. (2020), the

highest AWS on the Earth are installed adjacent to the Khumbu Glacier, Nepal. We use AWS observations to compute SEB described in Matthews et al. (2020). In our SEB modelling, turbulent fluxes are determined using the aerodynamic roughness at the glacier surface taken from measurements in low latitudes (Brock et al., 2006) and evaluated over the 5th to 95th percentile of this sample to capture uncertainty. Surface melting is defined by the glacier surface temperature~~s~~ (T_s) that is evolved from air temperature (T_a)~~s~~ and the residual downward glacier heat flux in the iterative approach from Wheler and Flowers (2011). Melting days are defined where $T_s = 0^oC$ at any point during the day. Supplementary information for this paper is provided to describe the SEB methodology in further detail (*Supplementary Information Section S1.1*).

A comparison of S1-SAR and SEB derived melting is shown in *Fig. 5*. During 2019, ~~the average~~ maximum daily T_a ~~air temperature~~ measurements at the Camp II station (*Fig. 5A*) reach ~~are never~~ above~~-~~zero temperatures starting June 13th and ending on September 11th. The maximum T_s ~~but experience above zero maximum glacier surface temperatures during starting~~ reaches 0^oC starting on ~~in~~ June 2nd ~~2019~~and ending on September 27th. ~~and ending in September 2019.~~ At the South Col AWS, the average temperature is much less, where maximum temperatures are never above melting and close to -10ºC on average during summer months (*Fig. 5B*). S1-SAR estimates of surface melting use two aggregated backscatter time-series over 90m x 90m areas where area centers are located nearest to each of the AWS stations over the Khumbu glacier, Nepal. For the Camp II AWS, this is centered at 6,483 m a.s.l. and for the South Col AWS, 7,128 m a.s.l. Melting signals are apparent at both Camp II (*Fig. 5C*) and South Col (*Fig. 5D*). A more robust comparison would match the timings of satellite overpasses and meteorological observations and acknowledge that some disagreement between melting estimates is resultant from this difference.

Melting is detected at high elevations in both SAR observations and SEB modelling output where daily average air temperatures remain below zero. We find that S1 and SEB estimates of surface melting at the Everest Camp II AWS (6,464 m a.s.l.) have an agreement score, the percentage of days where the SEB and SAR find the same condition, that ranges from 73% to 85% depending on the parameterization of surface roughness used in SEB estimates of melting. At Mt. Everest South Col (7,945 m a.s.l.) the agreement score varies from 63 to 68 percent. ~~We find that the~~ The S1-SAR record ~~finds~~ indicates 133 days of melting at Camp II while the SEB indicates from 93 to 100 days. At Mt. Everest South Col AWS the S1-SAR ~~finds~~ record indicates 72 days of melting while the SEB indicates 43 to 56. The start of surface melting at Camp II from SEB modeling is day of year (DOY) 153 and DOY 142 from S1-SAR, at South Col melt onset is DOY 152 from SEB and DOY 146 from S1-SAR. The end of surface melting at Camp II from SEB modeling is ~~day of year (~~DOY~~)~~ 270 and DOY 290 from S1-SAR. At South Col, refreeze at the surface from SEB is DOY 256 and DOY 244 from S1-SAR.

Using SEB outputs we find good agreement on surface melt timings, S1-SAR detects melt onset to within 9 days on average at two locations on the Khumbu Glacier in Nepal and refreeze to within 16 days. Although limited by observational data, the agreement in melt duration between S1-SAR and SEB modeling~~,~~ and the understanding of the physical basis of SAR measurements we have a high degree of confidence in our methodology and in the ability of the SAR backscatter to detect melting ~~and~~ in data-poor regions such as HMA.
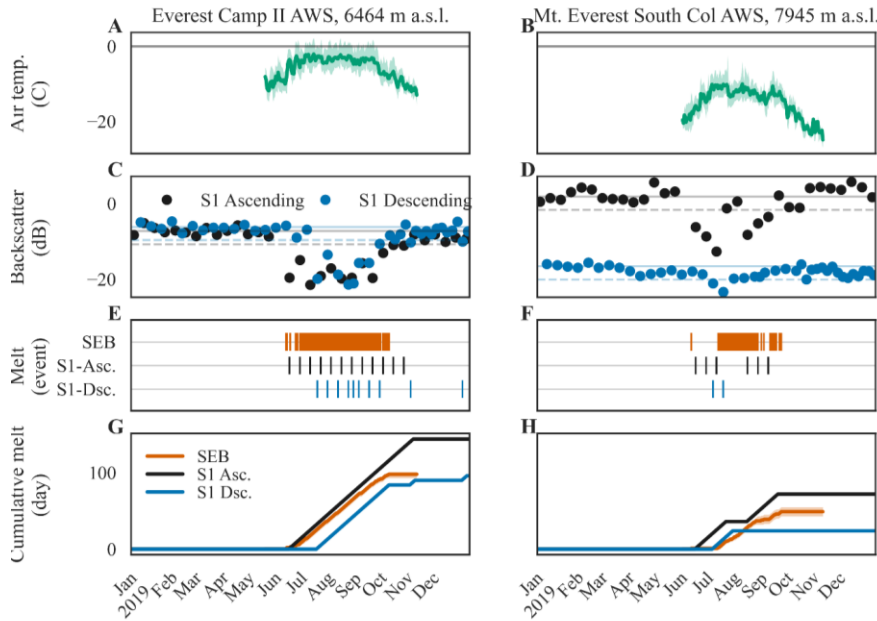
Figure 5. Average daily a-Air temperature measurements, with maximum and minimum (shaded) from (**A**) the Everest Camp II automated weather station (AWS) and (**B**) the Mt. Everest South Col AWS are compared to glacier surface melting observations from the Sentinel-1 satellite synthetic aperture radar (SAR). (**C**) The radar backscatter from the Khumbu Glacier (at 6,483 m a.s.l.) adjacent to the Camp II AWS, show a pronounced decrease in backscatter over several months associated with on-going surface melting during summer months. Melting is identified when backscatter decreases below a threshold (dashed-line), set at 3 dB below the winter mean (solid-line). (**D**) At the upper reaches of the Khumbu Glacier (7,128 m a.s.l.), S1-SAR observes melting during ascending passes (18:00 local time) but not during descending passes (06:00 local time) except for a brief period during late June., (**F**) Timing of surface melt from observation and SEB modeling are compared to S1 ascending and descending observations at (**E**) Camp II and (**F**) South Col AWS. The cumulative number of melting days from the SEB model and S1-SAR are shown for (**G**) Camp II and (**H**) South Col.

3.3 Comparison to temperature elevation lapse rates

Melting on glacier surfaces across the HKH is controlled by the SEB between the atmosphere and underlaying snow, firn or ice. We explore the relationship between the S1-SAR derived surface melting record and air temperature-elevation lapse rates within the Central Himalayas during 2018 using data from two meteorological stations within the Langtang Valley (*Table 2*). Temperature-elevation lapse rates were determined using three-day averages of hourly air temperature measurements interpolated to fill gaps using methods identical for the calculation of temperature elevation lapse rates in numerical model studies of snowmelt and glacier wasting in the HKH (Baral et al., 2014). We calculated the difference between three-day average air temperatures and divided by the difference in elevation (1,148 m) between the two stations in the Langtang River Valley, Nepal. Lapse-rates ranged from 5ºC

381 km^{-1} in July of 2018 to -13.7ºC km^{-1} in December of the same year. Temperature-elevation lapse rates were used to

382 extrapolate the maximum elevation of three isotherms (-10ºC, -5ºC, and 0ºC) for each day of year in 2018 in order to

383 compare extrapolated temperatures with melt retrievals from Sentinel-1.

384
385 **Table 2.** Sources of air temperature data used to calculate 3-day average temperature-elevation lapse rates within the
386 Central Himalaya for the 2018 calendar year.

STATION NAME	DATE RANGE (DD/MM/YYYY)	RESOLUTION	ELEVATION (M A.S.L.)	LATITUDE	LONGITUDE	SOURCE
YALA GLACIER	05/08/2012 – 12/31/2018	Hourly	4,950	28.23252	85.61208	ICIMOD
KYANGING STATION	03/22/2012 – 12/31/2019	Hourly	3,802	28.21081	85.56169	ICIMOD

387

388 **4 Results and Discussion**

389   A melting signal (**z** > 2) is observed across all mapped glacier area contained in the GAMDAM inventory.

390 Melt retrievals are aggregated across 17 glacio-climate sub-regions within the HKH delineated within the HiMAP

391 dataset (Shean et al., 2020) and averaged across the calendar years 2017-2019 to report summary statistics (*Table 3*).

392 Aggregate statistics of melt onset (MO) and freeze onset (FO) are calculated across 100m elevation bins using the

393 30m SRTM (Farr, 2007) digital elevation model for each glacio-climate sub-region as presented in *Figure 4*. For all

394 sub-regions, there is a roughly linear relationship of mean MO with elevation over most ranges in elevation. The

395 progression of MO with increasing elevation is consistent with lapse rate temperature controls on surface melting for

396 most elevation ranges. Notably, we find an inflection toward earlier melt onset occurring at higher elevations

397 (>6,500 m a.s.l.). A divergence from lapse-rate driven melting at high elevations suggests that snowmelt onset may

398 have regional triggers, like strong solar insolation (Matthews et al., 2019) or variable regional weather patterns; such

399 as increases in atmospheric moisture, cloudiness, and deep convection (Lau et al., 2010).

400   In the three years of freeze onset (FO) across sub-regions we do not find the level of elevation dependence

401 as observed in MO (*Fig. 6*). For much of the HKH, FO occurs during a short period of time and over large spans of

402 elevation. For example, in the Central Himalaya sub-region, FO has a range of 33 days while the MO for this region

403 spans 79 days on average. FO across sub-regions does not follow a linear trend with elevation similar to MO (*Fig.

404 6*). In western sub-regions (Eastern Hindu Kush, Western Pamir, and Karakoram), there is a signal of delayed

405 refreeze apparent in summary statistics at higher elevation ranges within each respective catchment. In the Western

406 Pamir, FO at 6,000 m occurs 22 days later than FO at 5,000m a.s.l (*Supplementary Fig. S2*). Similarly, in the

407 Karakoram, FO occurs 10 days later at 7,500 m a.s.l. compared to 6,500 m a.s.l. In the Tanggula Shan, FO at 6,500

408 m a.s.l. is delayed by 21 days relative to FO at 5,500 m a.s.l.

409   Signals of delayed refreeze are observed at elevation ranges similar to greatest **z**-score across each sub-

410 region. Complete refreeze across the depth of a percolation zone is delayed relative to percolation zone surfaces

411 because liquid water is retained within a percolation zone media after the surface of the percolation zone has frozen

412 (Paterson, 2016). Completely frozen percolation zones produce some of the largest radar backscatter responses on

413   the terrestrial earth (Jezek et al., 1994). Because frozen snow and percolation facies are essentially transparent, C-

414   band SAR will be sensitive to the presence of liquid water across the volume of a snowpack or firn strata (Fischer et

415   al., 2019). Signals of delayed refreeze across sub-regions are indicative of meltwater storage within the percolation

416   volume due to meltwater retention. A figure illustrating melt timings and **z**-score metric is included as

417   Supplementary materials (*Supplementary Fig. S2*).
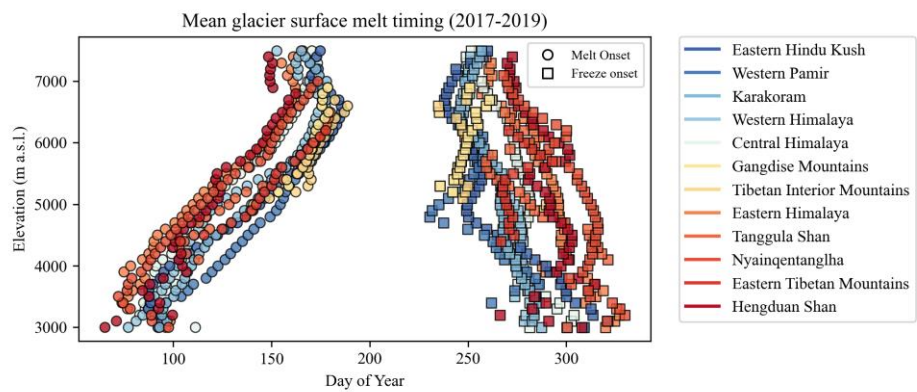
418
419   **Figure 6**. Mean melt onset (MO) and freeze onset (FO) summarized in 100m elevation bins using the 30m SRTM
420   digital elevation model (Farr, 2007) and 12 HiMAP sub-regions (Shean, 2020). The blue to red color scale indicates
421   the longitude of the HiMAP region centroid, where the westernmost regions are shown in dark blue and easternmost
422   shown in dark red.
423

424
425
426
427
428
429
430
431
432
433
434
435
436
437
438
439
440

Table 3. Melt retrieval statistics summarized across HiMAP sub-regions and aggregated over 1km elevation bins from the SRTM 30m DEM. Data for each elevation bin and sub-region are structured where the first row is the melt onset (MO) in day of year (DOY) and associated MO variance in days, freeze onset (DOY) and associated variance (days), and the area of melt retrieved in units of square kilometers.

Nyainge-ntanglha	Karako-ram	Hengduan Shan	Gangdise	Eastern Tibetan	Eastern Hindu Kush	Eastern Himalaya	Central Himalaya
79 (19)	105 (19)	90 (27)	-	-	101 (13)	75 (17)	90 (21)
300 (38)	278 (23)	294 (39)	-	-	276 (42)	293 (46)	277 (22)
145	955	11	-	-	89	25	49
105 (13)	128 (20)	113 (17)	-	136 (10)	131 (17)	102 (20)	104 (17)
310 (18)	268 (19)	294 (21)	-	268 (12)	257 (27)	292 (24)	274 (14)
2637	5889	231	-	26	2179	353	1492
131 (18)	152 (15)	121 (24)	164 (14)	151 (10)	152 (12)	129 (18)	134 (20)
302 (24)	262 (19)	289 (24)	247 (11)	275 (15)	253 (16)	290 (20)	274 (17)
5253	15060	1245	1123	381	1333	2621	7374
150 (11)	170 (17)	146 (15)	166 (10)	173 (7)	180 (13)	152 (13)	156 (12)
294 (22)	249 (13)	289 (16)	250 (9)	280 (5)	243 (10)	279 (18)	268 (15)
295	2752	43	438	4	177	774	2303
167 (9)	171 (20)	151 (5)	177 (-)	-	175 (20)	161 (12)	169 (13)
269 (4)	248 (12)	269 (7)	258 (-)	-	243 (13)	260 (12)	249 (14)
1	110	1	<1	-	11	22	153

Formatted Table

Elevation Range (m a.s.l.)	Western Pamir	Western Himalaya	Tibetan Interior	Tangg-ula Shan
3000-3999	117 (20)	94 (9)	-	-
	275 (28)	280 (22)	-	-
	602	156	-	-
4000 - 4999	141 (16)	113 (14)	136 (1)	120 (13)
	255 (23)	275 (15)	299 (11)	290 (14)
	5271	3651	<1	17
5000 - 5999	159 (12)	138 (20)	166 (11)	161 (13)
	250 (16)	263 (22)	249 (14)	265 (20)
	4103	6135	3109	2184
6000 - 6999	177 (13)	163 (11)	172 (12)	169 (9)
	243 (12)	247 (13)	249 (12)	284 (29)
	117	357	1634	112
7000 - 7999	170 (9)	162 (18)	-	-
	249 (8)	250 (10)	-	-
	2	13	-	-

Formatted Table

Formatted Table

4.1 Percolation Meltwater Hydrology

Delayed freeze-up apparent in summary statistics at unique elevation ranges across glacio-climate sub-regions is an important illustration of how melt retrievals from Sentinel-1 are sensitive to the presence of liquid water within the snowpack and/or firn subsurface (Brangers et al.; Fischer et al., 2019). At the Khumbu glacier on Mount Everest, Sentinel-1 retrieved refreeze occurs over thirty days later at ~6,000m a.s.l. compared to elevations below 5,400m a.s.l. and above 6,200m a.s.l., indicating that liquid meltwater was retained at elevation ranges between ~5,400-6,200m a.s.l. during a month when elevations both above and below this range were recorded as completely frozen within Sentinel-1 retrieved melt signals. The time series of mean Sentinel-1 SAR backscatter for descending orbital nodes from two 250m buffered points on the Khumbu glacier show a rapid increase in SAR backscatter magnitude for the higher elevation location, whereas backscatter time series extracted from within the elevation range of delayed melt offset show a gradual increase in radar backscatter. We interpret this gradual backscatter increase to be indicative of gradually decreasing liquid water content in the snowpack (or firn) as refreeze progresses from the glacier surface and into the depth of the percolation zone (*Fig. 7*) (Forster et al., 2014; Miège et al., 2016). This elevation range (~5,400-6,200 m a.s.l.) is similar to known elevation ranges of percolation zones on the Khumbu glacier as detailed in recent field work (Matthews et al., 2019; Matthews et al., 2020). SAR backscatter time series showing a gradual increase in backscatter within regions of known percolation suggest that a relationship between frozen percolation zone depth and the rate of C-band backscatter change across refreeze cycles. It has been shown that C-band backscatter gradually increases with frozen percolation zone depth and decreasing percolation zone wetness during a refreeze process (Ashcraft and Long, 2005).
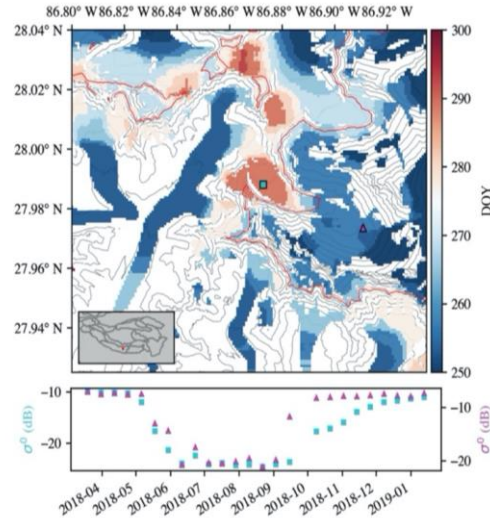
465
466 **Figure 7**. **(Top)** Refreeze timing over Khumbu glacier region of Mount Everest in the Central Himalaya. Red
467 regions of freeze onset occur at mid-elevations, indicative of delayed refreeze due to meltwater retention in
468 percolation zones. **(Bottom)** Sentinel-1 backscatter time series from two points on the Khumbu glacier, one within
469 known elevations of glacier percolation facies (teal square, 6,000 m a.s.l.) and another point at elevations where
470 temperatures likely do not exceed 0ºC annually (pink triangle, 6,600 m a.s.l.).
471

4.2   Spatial Variability: Radar Scattering and Glacier Facies

473   Imaging radar backscatter intensity, and response to surface melting, is linked with glacier facies (Ramage

474 et al., 2000; Rau et al., 2000; Zhou and Zheng, 2017). Snow melting on the glacier surface produces a strong

475 decrease in radar backscatter across all glacier facies. In the accumulation zone the refreeze signal is also

476 pronounced as the dissipation of strongly absorbing wet snow at the surface is followed by volume scattering from

477 deep snowpack and stratified ice layering. The scattering response to refreeze in the ablation zone is more complex

478 and not well characterized. Here, supra-glacier features like crevasses, sun-cups, debris-cover, and other

479 heterogeneities are likely to cause highly variable radar scattering mechanisms over short distances upon the

480 disappearance of snow from the ablation surface. (Rott and Mätzler, 1987). We use the **z**-score metric to select areas

481 where radar backscatter increases substantially during the refreeze process. However, since scattering response

482 during the transition from wet snow will differ with various surface features (e.g. bare ice, debris and supra-glacier

483 ponding) it is difficult to isolate the refreeze response. Average **z** is minimum in the HKH across the lowest

484 elevation glacier surfaces (2,000m-4,000m a.s.l.) whereas **z** is maximum at unique elevation ranges within sub-

485 regions (*Fig. 4, Supplementary Fig. S2.*). Ablation zone surfaces (at lower elevations) do not exhibit the magnitude

486 of backscatter intensity of percolation zones and therefore lower glaciated elevations show lesser seasonal contrast

487 than higher elevations. These differences are also apparent in the spatial granularity of melt retrievals from the S1-

488 SAR product, as shown in *Fig. 8*. Ablation zone surfaces on valley glaciers show spatial heterogeneity in MO

489   indicative of supraglacial features, like debris cover, rather than randomly distributed noise. There exists uncertainty

490   in the FO signal on glacier ablation surfaces that will require further investigation. In ablation areas with lower

491   sensitivity to melting, we hypothesize that snow-off conditions result in ~~brightening~~ increase of radar backscatter ~~of~~

492   ~~the radar signal~~ due to contributions to ~~surface~~ scattering ~~contributions~~ from wet debris, bare ice, or other ablation

493   surface heterogeneities related to ~~~~rough surface scattering. For this reason, at lower elevations where annual air

494   temperatures exceed 0ºC (i.e. where temperature-elevation lapse rates hold), lapse rate estimates of elevation might

495   be more robust estimates of FO using this approach. Overall, surface melting signals appear to be consistent with

496   expectations of temperature lapse rates (i.e. earlier melting and later refreeze at lower elevations) across elevations

497   where annual air temperatures likely exceed 0ºC (<6,000 m a.s.l.). We have illustrated the spatial granularity of melt

498   retrievals in *Fig. 8* in addition to average melt onset and offset by sub-region in *Fig. 9*.

499
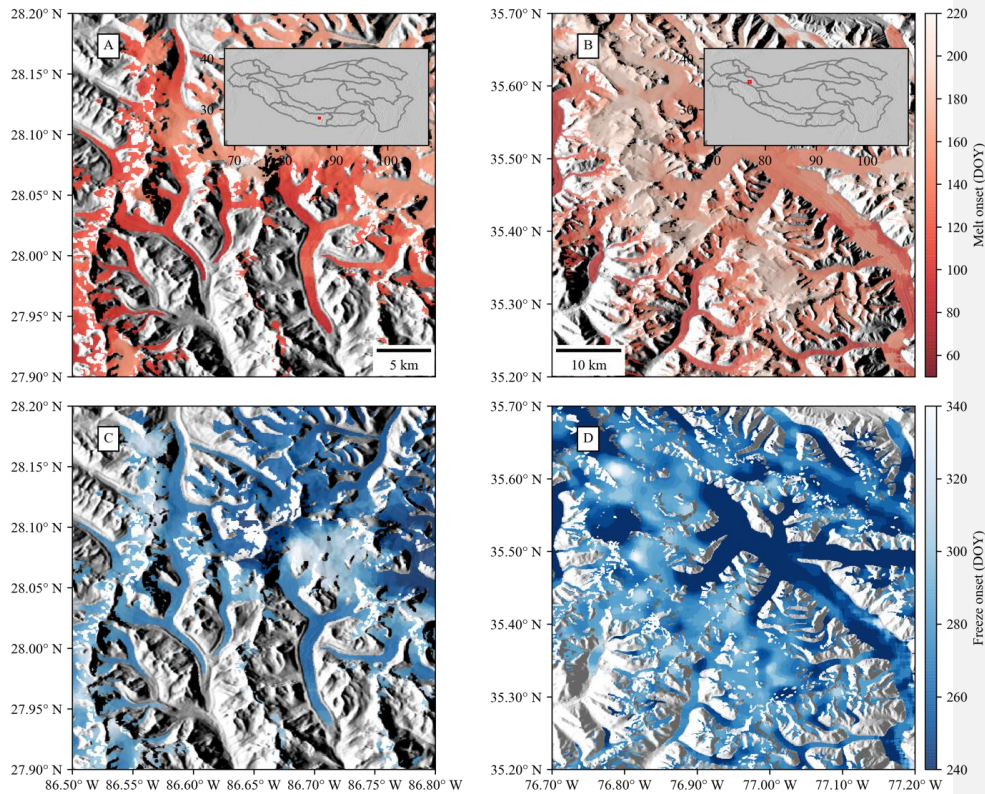
500
501 **Figure 8.** Melt retrievals averaged over the calendar years 2017-2019 in the Central Himalaya and Karakoram
502 regions. **(A)** Mean melt onset (DOY) in the Central Himalaya. **(B)** Mean melt onset (DOY) over the Siachen glacier
503 in the Karakoram region. **(C)** Mean melt offset (DOY) in the Central Himalaya. **(D)** Mean melt offset (DOY) over
504 the Siachen glacier in the Karakoram region.

505

506
507 **Figure 9**. Melt onset (top) and freeze onset (bottom) averaged over 2017-2019 plotted over a SRTM 30m DEM
508 hillshade (Farr, 2007). Melt retrievals are averaged across HiMAP glacio-climate sub-regions (Bolch et al., 2019a;
509 Shean et al., 2020) and scaled by the mapped glacier area within each sub-region.
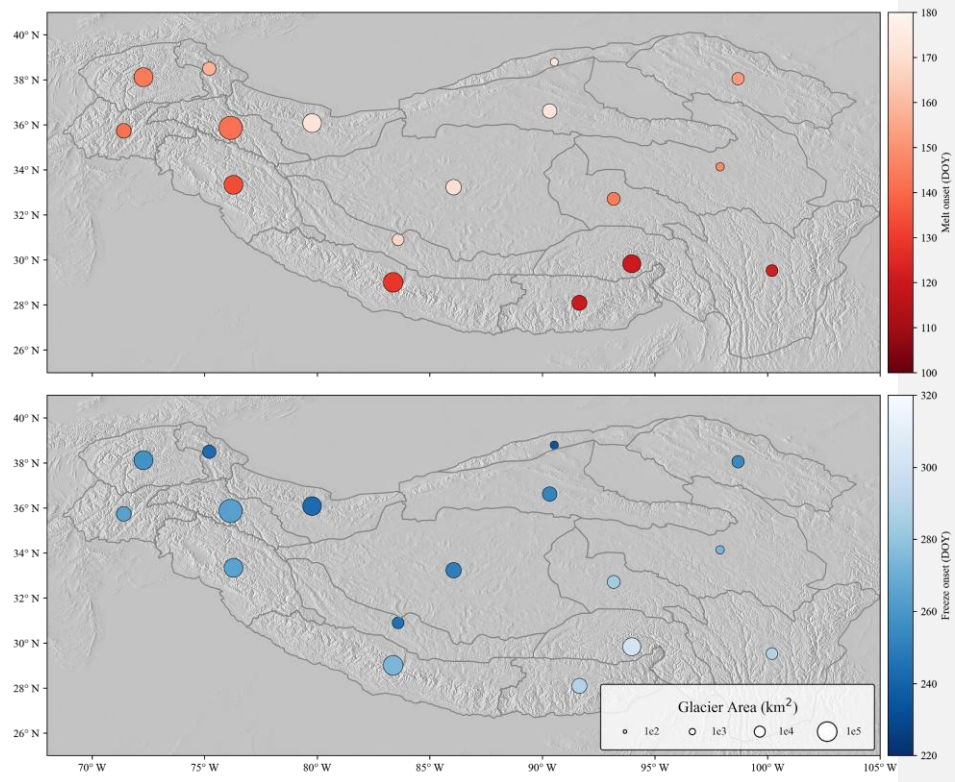
510
511
512
513
514
515
516
517
518
519
520
521
522

   4.3   Considerations of Temperature-Elevation Lapse Rates

524
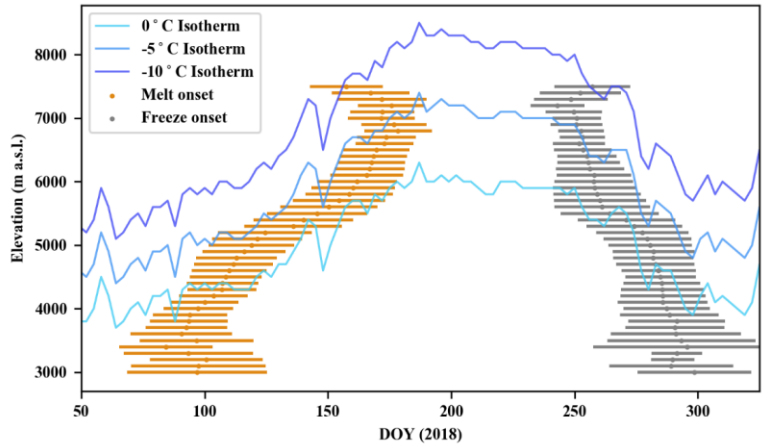
525
526   **Figure 7.** Sentinel-1 SAR retrieved melt onset (orange) and freeze onset (gray), with spatial variability at ±1
527   standard deviation, across the Central Himalaya region. The elevations of the 0°C, -5°C, and -10°C isotherms from
528   2018 are overlaid for comparison. Melt signals are recorded in excess of three months at elevations extending >1km
529   above the maximum elevation of the 0°C isotherm, indicative of a sustained presence of liquid water within the
530   snow matrix across these high elevation ranges.

531   We compare SAR retrievals of MO and FO to temperature-elevation lapse rates derived within a catchment

532   in the Central Himalaya to investigate SAR retrievals alongside lapse-rate assumptions of glacier melt status; using

533   methods and AWS data for the construction of lapse-rates from prior studies in the Langtang valley, Central

534   Himalaya (Baral et al., 2014). In 2018, we observe that the average MO is found to follow the 0° and -5ºC isotherms

535   for elevations ~4,500 to 6,500m a.s.l. Below and above these elevations, and for FO, we find episodic melting

536   events occurring over a range of elevations. This is especially apparent in the FO around day of year 270 where FO

537   occurs within a roughly two week period across glaciers between 5,000m-7,500m a.s.l. MO and FO signals are

538   retrieved on days and at elevations where lapse-rate derived temperatures do not exceed -10ºC, which strengthens

539   and expands recent *in situ* observations on glacier melt at the Khumbu glacier in the Mount Everest region showing

540   incident shortwave radiation drives melt at these temperatures and elevations (Matthews et al., 2019). Here we

541   observe that, even at these extreme elevations (>7,000m a.s.l.) melt signals persist for over three months on average

542   across the Central Himalaya, which suggests that liquid water is retained at these high elevations across a seasonal

543   melt cycle and may not be hydrologically negligible. In radar-derived observations there is a discrepancy between

544   SAR and lapse-rate estimated melting records that occurs at elevations extending 1km above the maximum 0ºC

545   isotherms in the Central Himalaya. Glaciated areas in the Central Himalaya at elevations greater than 6,000m a.s.l. –

546   the approximate maximum elevation of the 0ºC isotherm for 2018 – account for 21.58% (2,453 km^2) of total

547   glaciated area within the region.

548

4.4   Melt Retrievals and Glacio-Climate Sub-regions

549

550   The three-year record of Sentinel-1 SAR retrievals of glacier melt status represent a baseline measurement
551   for the HMA. The summary melt statistics are aggregated over HiMAP sub-regions in order to compare melt
552   retrievals and sub-regional estimates of glacier mass wasting (Bolch, et al. 2019a; Shean, et al., 2020). Overall, the
553   HMA sub-regions with the most rapid mass wasting between 2000-2010 tabulated in Shean, et al. (2019a) (Eastern
554   Himalaya, Hengduan Shan, Nyainquntanglha) exhibit the greatest number of melt days on average in 2017-2019
555   from Sentinel-1 retrievals. Sub-regions with slower mass wasting, in steady state, or with mass slight gain (Eastern
556   Hindu Kush, Western Pamir, Karakoram, Tibetan Interior) show on average one month less of melt duration relative
557   to regions with accelerated mass wasting. Interestingly, the Gangdise sub-region, with one of the higher post-2000
558   rates of glacier wasting in the HKH, shows annual melt durations of less than three months on average, which
559   appears more characteristic of western regions with slower mass wasting (i.e. Tibetan Interior Mountains). Although
560   Sentinel-1 retrievals of glacier melt status for three calendar years does not make-up a climatic record, we observe
561   that between 2017-2019 there was on average less duration of melting in regions where *in situ* data and climate
562   models indicate that frozen winter precipitation contributes to glacier accumulation despite warming global climate
563   (Karakoram, Hindu Kush, Eastern Pamir, Western Himalaya) (Kääb et al., 2015; Kapnick et al., 2014; Palazzi et al.,
564   2013). We interpret shorter duration of annual melt days in the western regions of the HKH as a potential indicator
565   of the "Karakoram Anomaly" reflected in the Sentinel-1 data record. Because the meteo-climatic drivers of the
566   Karakoram Anomaly are still under debate (Farinotti et al., 2020), Sentinel-1 retrievals of melt duration may be
567   useful for interrogating meteo-climatic drivers of heterogeneity in glacier wasting dynamics across the HKH.

5   Conclusion

568

569   Synthetic aperture radar time series backscatter images and glacier extent maps derived from optical imagery
570   have long been proposed to inform hydrologic and glaciologic research across the global cryosphere, however a
571   harmonized dataset of glacier surface melt does not exist. We retrieve glacier surface melt timing and duration for
572   the study years 2017-19 across the HKH region using time series C-band SAR from the Sentinel-1 A/B satellites and
573   an inventory of 105,432 glaciers spanning 83,102 km^2 of ice-covered area. We quantify the magnitude of the
574   seasonal melt signal by comparing mean summer and winter backscatter using a **z**-score metric and retrieve
575   constraints on seasonal melt characteristics across all glaciated elevations of HKH at 90m spatial and 12-day
576   temporal resolution. Melt conditions in surface energy balance models of glacier melt driven by *in situ*
577   meteorological data from Mount Everest are constrained by Sentinel-1 SAR melt retrievals. Comparison of melt
578   retrievals to temperature-elevation lapse rates calculated using two high-elevation meteorological stations in the
579   Central Himalaya reveal that melt onset persists for over three months at elevations where extrapolated air
580   temperature fields do not exceed -10°C. Melt is retrieved across all elevation ranges of HKH glaciers, which
581   suggests that a dry snow accumulation zone in the HKH region does not exist. Meltwater retention is indicated
582   within known glacier percolation zones on Mount Everest through signals of delayed refreeze. Delayed refreeze

583 occurs across the HKH at elevations with the greatest seasonal contrast in backscatter intensity, attributable to radar
584 scattering in percolation facies. Melt signals persist for a greater portion of the year in regions known for rapid
585 contemporary glacier wasting (i.e. Central and Eastern Himalaya sub-regions) whereas regions with stable glacier
586 mass balance (i.e. Karakoram) exhibit a shorter duration of annual melt. We produce a geospatial data product of
587 melt onset (DOY) and freeze onset (DOY) spanning glaciers of the HKH region at 90m spatial resolution for the
588 calendar years 2017-2019 and plan to release annual updates to this dataset each calendar year across the mission
589 duration of Sentinel-1. The methods presented in this study can provide the basis for an operational monitor of
590 glacier surface melt dynamics and aid the development and assessment of surface energy balance models of glacier
591 ablation across the global cryosphere.

6   Acknowledgements

593 This work was supported by funds provided to The City College of New York by the National Aeronautics and
594 Space Administration Cryosphere Program's High Mountain Asia Team (HiMAT) program, under award number
595 NNX16AQ83G. Portions of this work were conducted at the Jet Propulsion Laboratory, California Institute of
596 Technology, under contract to the National Aeronautics and Space Administration.

Author Contribution

598
599 N. C. Steiner and K. C. McDonald devised the project and the main conceptual ideas. C. Scher developed and
600 executed the 425 final methodological approach and authored the computer code. C.S contributed most of the
601 writing to the manuscript with major contributions from N.C.S. K.C.M supervised the project and manuscript.

Competing Interest

603 The authors declare no competing interests.

Code and Data availability

605 The code and data will be available on in the NASA Distributed Active Archive Center, the National Snow and Ice
606 Data Center, as part of the High Mountain Asia Data archive.

7   References

608 Abdalati, W. and Steffen, K.: Greenland Ice Sheet melt extent: 1979-1999, Journal of Geophysical Research:
609 Atmospheres, 106, 33983-33988, 2001.
610
611 Adam, S., Pietroniro, A., and Brugman, M. M.: Glacier snow line mapping using ERS-1 SAR imagery, Remote
612 Sensing of Environment, 61, 46-54, 1997.

613
614 Alexander, P., Tedesco, M., Koenig, L., and Fettweis, X.: Evaluating a regional climate model simulation of
615 Greenland ice sheet snow and firn density for improved surface mass balance estimates, Geophysical Research
616 Letters, 46, 12073-12082, 2019.
617
618 Anthwal, A., Joshi, V., Sharma, A., and Anthwal, S.: Retreat of Himalayan glaciers–indicator of climate change,
619 Nature and Science, 4, 53-59, 2006.
620
621 Ashcraft, I. S. and Long, D. G.: Comparison of methods for melt detection over Greenland using active and passive
622 microwave measurements, International Journal of Remote Sensing, 27, 2469-2488, 2007.
623
624 Ashcraft, I. S. and Long, D. G.: Differentiation between melt and freeze stages of the melt cycle using SSM/I
625 channel ratios, IEEE transactions on geoscience and remote sensing, 43, 1317-1323, 2005.
626
627 Baghdadi, N., Gauthier, Y., and Bernier, M.: Capability of multitemporal ERS-1 SAR data for wet-snow mapping,
628 Remote sensing of environment, 60, 174-186, 1997.
629
630 Bahr, D. B., Meier, M. F., and Peckham, S. D.: The physical basis of glacier volume-area scaling, Journal of
631 Geophysical Research: Solid Earth, 102, 20355-20362, 1997.
632
633 Baral, P., Kayastha, R. B., Immerzeel, W. W., Pradhananga, N. S., Bhattarai, B. C., Shahi, S., Galos, S., Springer,
634 C., Joshi, S. P., and Mool, P. K.: Preliminary results of mass-balance observations of Yala Glacier and analysis of
635 temperature and precipitation gradients in Langtang Valley, Nepal, Annals of glaciology, 55, 9-14, 2014.
636
637 Bhattacharya, I., Jezek, K. C., Wang, L., and Liu, H.: Surface melt area variability of the Greenland ice sheet: 1979–
638 2008, Geophysical Research Letters, 36, 2009.
639
640 Bindschadler, R., Jezek, K., and Crawford, J.: Glaciological investigations using the synthetic aperture radar
641 imaging system, Annals of Glaciology, 9, 11-19, 1987.
642
643 Bogardi, J. J., Dudgeon, D., Lawford, R., Flinkerbusch, E., Meyn, A., Pahl-Wostl, C., Vielhauer, K., and
644 Vörösmarty, C.: Water security for a planet under pressure: interconnected challenges of a changing world call for
645 sustainable solutions, Current Opinion in Environmental Sustainability, 4, 35-43, 2012.
646
647 Bolch, T., Shea, J. M., Liu, S., Azam, F. M., Gao, Y., Gruber, S., Immerzeel, W. W., Kulkarni, A., Li, H., and Tahir,
648 A. A.: Status and change of the cryosphere in the Extended Hindu Kush Himalaya Region. In: The Hindu Kush
649 Himalaya Assessment, Springer, 2019a.
650
651 Bolch, T., Kulkarni, A., Kääb, A., Huggel, C., Paul, F., Cogley, J. G., Frey, H., Kargel, J. S., Fujita, K., and Scheel,
652 M. J. S.: The state and fate of Himalayan glaciers, 336, 310-314, 2012.
653
654 Bolch, T., Bhattacharya, A., King, O., and Allen, S.: Characteristics and changes of glaciers, rock glaciers and
655 glacial lakes in High Mountain Asia since the 1960s, 2019b.
656
657 Brangers, I., Lievens, H., Miège, C., Demuzere, M., Brucker, L., and De Lannoy, G.: Sentinel-1 detects firn aquifers
658 in the Greenland Ice Sheet, Geophysical Research Letters.
659
660 Brock, B. W., Willis, I. C., and Sharp, M. J.: Measurement and parameterization of aerodynamic roughness length
661 variations at Haut Glacier d'Arolla, Switzerland, Journal of Glaciology, 52, 281-297, 2006.
662
663 Brown, L. E., Hannah, D. M., and Milner, A. M.: Vulnerability of alpine stream biodiversity to shrinking glaciers
664 and snowpacks, Global Change Biology, 13, 958-966, 2007.
665
666 Brun, F., Berthier, E., Wagnon, P., Kaab, A., and Treichler, D.: A spatially resolved estimate of High Mountain Asia
667 glacier mass balances, 2000-2016, Nat Geosci, 10, 668-673, 2017.
668

Carrivick, J. L. and Tweed, F. S.: A global assessment of the societal impacts of glacier outburst floods, Global and Planetary Change, 144, 1-16, 2016.

Engeset, R., Kohler, J., Melvold, K., and Lundén, B.: Change detection and monitoring of glacier mass balance and facies using ERS SAR winter images over Svalbard, International Journal of Remote Sensing, 23, 2023-2050, 2002. ESA: https://sentinel.esa.int/web/sentinel/user-guides/sentinel-1-sar/acquisition-modes/interferometric-wide-swath, last access: February 13, 2020.

Farinotti, D., Immerzeel, W. W., de Kok, R. J., Quincey, D. J., and Dehecq, A.: Manifestations and mechanisms of the Karakoram glacier Anomaly, Nature Geoscience, 13, 8-16, 2020.

Farr, T. G., Rosen, P.A., Caro, E., Crippen, R., Duren, R., Hensley, S., Kobrick, M., Paller, M., Rodriguez, E., Roth, L., Seal, D., Shaffer, S., Shimada, J., Umland, J., Werner, M., Oskin, M., Burbank, D., and Alsdorf, D.E.: The shuttle radar topography mission: Reviews of Geophysics, v. 45, no. 2, RG2004, at https://doi.org/10.1029/2005RG000183., Reviews of Geophysics, 45, 2007.

Fischer, G., Jäger, M., Papathanassiou, K. P., and Hajnsek, I.: Modeling the Vertical Backscattering Distribution in the Percolation Zone of the Greenland Ice Sheet with SAR Tomography, IEEE Journal of Selected Topics in Applied Earth Observations and Remote Sensing, 12, 4389-4405, 2019.

Fujita, K. and Nuimura, T.: Spatially heterogeneous wastage of Himalayan glaciers, Proc Natl Acad Sci U S A, 108, 14011-14014, 2011.

Gardelle, J., Berthier, E., and Arnaud, Y.: Slight mass gain of Karakoram glaciers in the early twenty-first century, Nature geoscience, 5, 322, 2012.

Google: Sentinel-1 Preprocessing, last access: Novermber 30, 2020 2020.

Gorelick, N., Hancher, M., Dixon, M., Ilyushchenko, S., Thau, D., and Moore, R. J. R. S. o. E.: Google Earth Engine: Planetary-scale geospatial analysis for everyone, 202, 18-27, 2017.

Hallikainen, M., Ulaby, F., and Abdelrazik, M.: Dielectric properties of snow in the 3 to 37 GHz range, IEEE transactions on Antennas and Propagation, 34, 1329-1340, 1986.

Huang, L., Li, Z., Tian, B.-S., Chen, Q., Liu, J.-L., and Zhang, R.: Classification and snow line detection for glacial areas using the polarimetric SAR image, Remote Sensing of Environment, 115, 1721-1732, 2011.

Huang, W., DeVries, B., Huang, C., Lang, M., Jones, J., Creed, I., and Carroll, M.: Automated Extraction of Surface Water Extent from Sentinel-1 Data, Remote Sensing, 10, 2018.

ICIMOD: Outline Boundary of Hindu Kush Himalayan (HKH) Region. ICIMOD (Ed.), ICIMOD.
Jacobsen, D., Milner, A. M., Brown, L. E., and Dangles, O.: Biodiversity under threat in glacier-fed river systems, Nature Climate Change, 2, 361, 2012.

Jezek, K. C., Gogineni, P., and Shanableh, M.: Radar measurements of melt zones on the Greenland ice sheet, Geophysical Research Letters, 21, 33-36, 1994.

Kääb, A., Treichler, D., Nuth, C., and Berthier, E.: Brief Communication: Contending estimates of 2003–2008 glacier mass balance over the Pamir–Karakoram–Himalaya, Cryosphere, 9, 2015.

Kapnick, S. B., Delworth, T. L., Ashfaq, M., Malyshev, S., and Milly, P. C.: Snowfall less sensitive to warming in Karakoram than in Himalayas due to a unique seasonal cycle, Nature Geoscience, 7, 834, 2014.
Kayastha, R. B., Steiner, N., Kayastha, R., Mishra, S. K., and McDonald, K.: Comparative study of hydrology and icemelt in three Nepal river basins using the glacio-hydrological degree-day model (GDM) and observations from the Advance Scatterometer (ASCAT), FrEaS, 7, 354, 2019.

Kendra, J. R., Sarabandi, K., Ulaby, F. T. J. I. T. o. G., and Sensing, R.: Radar measurements of snow: Experiment and analysis, 36, 864-879, 1998.

Koskinen, J. T., Pulliainen, J. T., and Hallikainen, M. T.: The use of ERS-1 SAR data in snow melt monitoring, IEEE Transactions on geoscience and remote sensing, 35, 601-610, 1997.

Lau, W. K., Kim, M.-K., Kim, K.-M., and Lee, W.-S.: Enhanced surface warming and accelerated snow melt in the Himalayas and Tibetan Plateau induced by absorbing aerosols, Environmental Research Letters, 5, 025204, 2010.

Lievens, H., Demuzere, M., Marshall, H.-P., Reichle, R. H., Brucker, L., Brangers, I., de Rosnay, P., Dumont, M., Girotto, M., and Immerzeel, W. W.: Snow depth variability in the Northern Hemisphere mountains observed from space, Nature communications, 10, 1-12, 2019.

Litt, M., Shea, J., Wagnon, P., Steiner, J., Koch, I., Stigter, E., and Immerzeel, W.: Glacier ablation and temperature indexed melt models in the Nepalese Himalaya, Scientific reports, 9, 5264, 2019.

Lund, J., Forster, R. R., Rupper, S. B., Marshall, H., Deeb, E. J., and Hashmi, M. Z. U. R.: Mapping snowmelt progression in the Upper Indus Basin with synthetic aperture radar, Frontiers in Earth Science, 7, 318, 2019.
Margulis, S. A., Liu, Y., and Baldo, E.: A joint Landsat-and MODIS-based reanalysis approach for midlatitude montane seasonal snow characterization, Frontiers in Earth Science, 7, 272, 2019.

Matthews, T., Perry, B., Aryal, D., Shrestha, D., and Khadka, A.: New Heights in Glacier-Climate Research: Initial Insights From the Highest Weather Stations on Earth, 2019.

Matthews, T., Perry, L. B., Koch, I., Aryal, D., Khadka, A., Shrestha, D., Abernathy, K., Elmore, A., Seimon, A., and Tait, A.: Going to Extremes: Installing the World's Highest Weather Stations on Mount Everest, B Am Meteorol Soc, 2020. 2020.

Matzler, C.: Microwave properties of ice and snow. In: Solar System Ices, Springer, 1998.

Miles, K. E., Hubbard, B., Quincey, D. J., Miles, E. S., Sherpa, T. C., Rowan, A. V., and Doyle, S. H.: Polythermal structure of a Himalayan debris-covered glacier revealed by borehole thermometry, Scientific reports, 8, 1-9, 2018.

Milner, A. M., Khamis, K., Battin, T. J., Brittain, J. E., Barrand, N. E., Fureder, L., Cauvy-Fraunie, S., Gislason, G. M., Jacobsen, D., Hannah, D. M., Hodson, A. J., Hood, E., Lencioni, V., Olafsson, J. S., Robinson, C. T., Tranter, M., and Brown, L. E.: Glacier shrinkage driving global changes in downstream systems, Proc Natl Acad Sci U S A, 114, 9770-9778, 2017.

Nagler, T. and Rott, H.: Retrieval of wet snow by means of multitemporal SAR data, IEEE Transactions on Geoscience and Remote Sensing, 38, 754-765, 2000.

Nagler, T., Rott, H., Ripper, E., Bippus, G., and Hetzenecker, M.: Advancements for Snowmelt Monitoring by Means of Sentinel-1 SAR, Remote Sensing, 8, 348, 2016.

Nuimura, T., Sakai, A., Taniguchi, K., Nagai, H., Lamsal, D., Tsutaki, S., Kozawa, A., Hoshina, Y., Takenaka, S., and Omiya, S.: The gamdam glacier inventory: a quality-controlled inventory of Asian glaciers, Cryosphere, 9, 2015.

Oza, S., Singh, R., Vyas, N., and Sarkar, A.: Study of inter-annual variations in surface melting over Amery Ice Shelf, East Antarctica, using space-borne scatterometer data, Journal of earth system science, 120, 329-336, 2011.

Palazzi, E., Von Hardenberg, J., and Provenzale, A.: Precipitation in the Hindu-Kush Karakoram Himalaya: observations and future scenarios, Journal of Geophysical Research: Atmospheres, 118, 85-100, 2013.

Paterson, W. S. B.: The physics of glaciers, Elsevier, 2016.

781 Pritchard, D. M., Forsythe, N., O'Donnell, G., Fowler, H. J., and Rutter, N.: Multi-physics ensemble snow modelling
782 in the western Himalaya, The Cryosphere, 2020. 2020.

784 Ramage, J. M., Isacks, B. L., and Miller, M. M.: Radar glacier zones in southeast Alaska, USA: field and satellite
785 observations, Journal of Glaciology, 46, 287-296, 2000.

787 Rau, F., Braun, M., Friedrich, M., Weber, F., and Goßmann, H.: Radar glacier zones and their boundaries as
788 indicators of glacier mass balance and climatic variability, 2000, 317-327.

790 Rott, H. and Mätzler, C.: Possibilities and limits of synthetic aperture radar for snow and glacier surveying, Annals
791 of Glaciology, 9, 195-199, 1987.

793 Sakai, A.: Brief communication: Updated GAMDAM glacier inventory over high-mountain Asia, The Cryosphere,
794 13, 2043-2049, 2019.

796 Scott, C. A., Zhang, F., Mukherji, A., Immerzeel, W., Mustafa, D., and Bharati, L.: Water in the Hindu Kush
797 Himalaya. In: The Hindu Kush Himalaya Assessment, Springer, 2019.

799 Shea, J.: Meteorological data from Yala Base Camp automatic weather station. ICIMOD (Ed.), 2016.

801 Shean, D. E., Bhushan, S., Montesano, P., Rounce, D. R., Arendt, A., and Osmanoglu, B.: A Systematic, Regional
802 Assessment of High Mountain Asia Glacier Mass Balance, Frontiers in Earth Science, 7, 2020.

804 Shi, J. and Dozier, J.: Inferring snow wetness using C-band data from SIR-C's polarimetric synthetic aperture radar,
805 IEEE transactions on geoscience and remote sensing, 33, 905-914, 1995.

807 Shi, J., Dozier, J., and Rott, H.: Snow mapping in alpine regions with synthetic aperture radar, IEEE Transactions on
808 Geoscience and Remote Sensing, 32, 152-158, 1994.

810 Steiner, N. and Tedesco, M.: A wavelet melt detection algorithm applied to enhanced-resolution scatterometer data
811 over Antarctica (2000–2009), The Cryosphere, 8, 25-40, 2014.

813 Trusel, L. D., Frey, K. E., and Das, S. B.: Antarctic surface melting dynamics: Enhanced perspectives from radar
814 scatterometer data, Journal of Geophysical Research: Earth Surface, 117, 2012.

816 Winebrenner, D. P., Nelson, E. D., Colony, R., and West, R. D.: Observation of melt onset on multiyear Arctic sea
817 ice using the ERS 1 synthetic aperture radar, Journal of Geophysical Research, 99, 1994.

819 Winsvold, S., Kääb, A., Nuth, C., Andreassen, L. M., Van Pelt, W., and Schellenberger, T.: Using SAR data time-
820 series for regional glacier mapping, The Cryosphere, 12, 867-890, 2018.

822 Wiscombe, W. J. and Warren, S. G. J. J. o. t. A. S.: A model for the spectral albedo of snow. I: Pure snow, 37, 2712-
823 2733, 1980.

825 Wood, L. R., Neumann, K., Nicholson, K. N., Bird, B. W., Dowling, C. B., and Sharma, S.: Melting Himalayan
826 Glaciers Threaten Domestic Water Resources in the Mount Everest Region, Nepal, Frontiers in Earth Science, 8,
827 2020.

829 Yao, T., Thompson, L. G., Mosbrugger, V., Zhang, F., Ma, Y., Luo, T., Xu, B., Yang, X., Joswiak, D. R., and
830 Wang, W.: Third pole environment (TPE), Environmental Development, 3, 52-64, 2012.

832 Zemp, M., Haeberli, W., Hoelzle, M., and Paul, F.: Alpine glaciers to disappear within decades?, Geophysical
833 Research Letters, 33, 2006.
834

835 Zemp, M., Huss, M., Thibert, E., Eckert, N., McNabb, R., Huber, J., Barandun, M., Machguth, H., Nussbaumer, S.
836 U., and Gärtner-Roer, I.: Global glacier mass changes and their contributions to sea-level rise from 1961 to 2016,
837 Nature, 568, 382-386, 2019.
838
839 Zhou, C. and Zheng, L.: Mapping Radar Glacier Zones and Dry Snow Line in the Antarctic Peninsula Using
840 Sentinel-1 Images, Remote Sensing, 9, 2017.
841